INTERNATIONAL JOURNAL FOR NUMERICAL METHODS IN FLUIDS
Int. J. Numer. Meth. Fluids 2003; **43**:25–42 (DOI: 10.1002/fld.597)

A multigrid pseudospectral method for steady flow computation

Mo-Hong Chou*,†

Institute of Mathematics, Academia Sinica, Nankang, Taipei 11529, Taiwan

SUMMARY

In this work two-dimensional steady flow problems are cast into a fixed-point formulation, $Q = F(Q)$. The non-linear operator, F, is an approximate pseudospectral solver to the Navier–Stokes equations. To search the solution we employ Picard iteration together with a one-dimensional error minimization and a random perturbation in case of getting stuck. A monotone convergence is brought out, and is greatly improved by using a multigrid strategy. The efficacy of this approach is demonstrated by computing flow between eccentric rotating cylinders, and the regularized lid-driven cavity flow with Reynolds number up to 1000. Copyright © 2003 John Wiley & Sons, Ltd.

KEY WORDS: multigrid; Picard iteration; pseudospectral; random perturbation

1. INTRODUCTION

Incompressible steady flow computation is interesting in its own right. Among the several formulations of the Navier–Stokes equations the primitive variable approach is preferred by many researchers owing to its feasibility for both two- and three-dimensional problems. How to deal with the pressure term, or the incompressibility constraint, is the main difficulty associated with this approach. The artificial compressibility method as proposed by Chorin [1] is a marked scheme in conjunction with pseudo-unsteady simulations. If the steady flow is expected from real unsteady simulations, one has to devise a suitable boundary condition for solving the pressure Poisson equation. For two-dimensional settings the vorticity–streamfunction formulation, as adopted in this work, is an oft-cited alternative owing to its automatic satisfaction of incompressibility. However, there exists an asymmetric imposition of boundary conditions on vorticity and streamfunction.

As far as numerical approximations are concerned, most of the spatial discretization techniques such as finite-difference, finite-element, finite-volume, and spectral methods have been employed with success in different aspects. They are expounded in the books by Peyret and

*Correspondence to: Mo-Hong Chou, Institute of Mathematics, Academia Sinica, Nanking, Taipei 11529, Taiwan.
†E-mail: chou@math.sinica.edu.tw

Contract/grant sponsor: National Science Council; contract/grant number: NSC90-2115-M-001-011

Received 14 August 2002
Revised 14 April 2003

Taylor [2], Gresho and Sani [3], Ferziger and Perić [4], Canuto *et al.* [5], Peyret [6], to name but a few. We adopt the pseudospectral approach for its high order of accuracy and collocation feature in handling nonlinearity. Although the potential good accuracy suggests us to solve smaller systems of equations, they are however much more ill-conditioned than those obtained by lower order schemes like finite difference. Preconditioning in one form or another is needed if iterative methods are invoked.

We regard here the steady Navier–Stokes equations as two coupled Poisson equations for finding vorticity and streamfunction simultaneously. The coupling arises from the source terms and the overspecified boundary conditions for streamfunction. In our approach the convection part of the vorticity transport equation is treated as a trial source term, Q, to the vorticity Poisson equation. This quantity will be updated by a non-linear operator, $F(Q)$, if we carry out the coupled Poisson solver. Thus the goal is to find Q such that $F(Q)=Q$, a fixed-point formulation. As a consequence, the wanted solutions to vorticity and streamfunction are also fixed.

The construction of the operator, $F(Q)$, is detailed in Section 2. Via the fixed-point formulation, Picard iteration is a natural scheme for finding the solution. To be successful we incorporate it with a one-dimensional error minimization process. The performance can be greatly improved by putting the scheme into a multigrid fashion. We have demonstrated it recently [7] but in connection with a finite-difference approximation. The subtlety of $F(Q)$ is increased by pseudospectral approximation, and the above procedure is prone to get stuck, especially when the Reynolds number is not small. A random perturbation is introduced to sustain the line search, and the monotone convergence is recovered. The whole procedure is detailed in Section 3.

The efficacy of the proposed scheme is demonstrated in Section 4. We compute the steady flow between two eccentric cylinders rotating in several different modes. Such a configuration is interesting for lubrication studies, but is not standard for applying pseudospectral method. We also compute the regularized lid-driven cavity flow with Reynolds number up to 1000. Some comparisons with existing results are included.

2. PROBLEM FORMULATION

Consider a two-dimensional incompressible flow confined in a bounded region, $\tilde{\Omega}$, which can be simply or doubly connected. For applying pseudospectral discretization a standard domain, $\tilde{\Omega}=\Omega=[-1,1]\times[-1,1]$, is assumed if it is simply connected. Otherwise a smooth co-ordinate transformation, $(x,y)\mapsto(\xi,\eta)$, is introduced to turn a doubly connected $\tilde{\Omega}$ into a rectangular one, $\Omega=[0,2\pi]\times[-1,1]$. The boundaries or cutting lines of $\tilde{\Omega}$ corresponding to the top, bottom, left, and right edges of Ω will be denoted by $\Gamma_1,\Gamma_2,\Gamma_3$, and Γ_4, respectively. The flow is governed by the steady Navier–Stokes equations in terms of vorticity(ω) and streamfunction(ψ) as follows.

$$Re(\psi_y\omega_x-\psi_x\omega_y)=\omega_{xx}+\omega_{yy} \tag{1}$$

$$\psi_{xx}+\psi_{yy}=-\omega \quad \text{in } \Omega=\tilde{\Omega} \tag{2}$$

$$\psi=0 \quad \text{and } \partial\psi/\partial v=g, \quad \text{on } \partial\Omega=\bigcup_{i=1}^{4}\Gamma_i \tag{3}$$

In Equation (3) the normal derivative or Neumann condition, g, is prescribed. For doubly connected $\tilde{\Omega}$ these equations are transformed into the following:

$$Re(\psi_\eta \omega_\xi - \psi_\xi \omega_\eta) = (\alpha\omega_{\xi\xi} + \beta\omega_{\eta\eta} + \gamma\omega_{\xi\eta} + a\omega_\xi + b\omega_\eta)/J \tag{4}$$

$$(\alpha\psi_{\xi\xi} + \beta\psi_{\eta\eta} + \gamma\psi_{\xi\eta} + a\psi_\xi + b\psi_\eta)/J = -\omega/J \quad \text{in } \Omega \tag{5}$$

$$\psi(0,\eta) = \psi(2\pi,\eta) \quad \text{and } \omega(0,\eta) = \omega(2\pi,\eta) \quad \text{on } \Gamma_3 \cup \Gamma_4 \tag{6}$$

$$\psi = 0 \quad \text{on } \Gamma_1, \quad \psi = f \quad \text{on } \Gamma_2, \quad \text{and} \quad \partial\psi/\partial v = g \quad \text{on} \quad \Gamma_1 \cup \Gamma_2 \tag{7}$$

Unlike g, the Dirichlet constant, f, in Equation (7) is determined *a posteriori* by the integral conditions

$$\oint_{\Gamma_1} \partial\omega/\partial v = \oint_{\Gamma_2} \partial\omega/\partial v = 0 \tag{8}$$

They are equivalent to the univalence of pressure: $\oint \mathrm{d}p = 0$ around Γ_1 and Γ_2.

In Equations (4)–(5) we have the transformation's Jacobian: $J = |\partial(\xi,\eta)/\partial(x,y)|$, and the following relations:

$$\alpha = \xi_x^2 + \xi_y^2, \quad \beta = \eta_x^2 + \eta_y^2, \quad \gamma = 2(\xi_x\eta_x + \xi_y\eta_y), \quad a = \xi_{xx} + \xi_{yy}, \quad b = \eta_{xx} + \eta_{yy} \tag{9}$$

For simplicity, we shall assume the transformation is started by a conformal mapping, and continued by an independent remeshing in each spatial dimension. This will yield $\gamma = 0$, or the vanishing of the cross derivative term.

The unknowns, ω and ψ, are to be determined over the Chebyshev or Fourier collocation points depending on the boundary condition in each dimension. Their first and second derivatives are derived from the corresponding pseudospectral interpolants. Each multiplication or division is handled by means of collocation. These procedures are standard to pseudospectral methods, and are expounded, for example, in the books by Gottlieb and Orszag [8], Canuto *et al.* [5], and Fornberg [9].

Such an approximation to the Laplace operator appearing on the right-hand sides of Equations (1) and (4), as well as on the left-hand sides of Equations (2) and (5), results in a matrix, $\mathscr{L}$. The whole estimation of vorticity convection, $\psi_y\omega_x - \psi_x\omega_y$ and $\psi_\eta\omega_\xi - \psi_\xi\omega_\eta$ in Equations (1) and (4), respectively, is denoted by Q for the time being, and the Navier–Stokes equations are formally reexpressed as a system of two coupled Poisson equations:

$$Re \cdot Q = \mathscr{L}\omega, \quad \mathscr{L}\psi = -\omega/J \quad \text{in} \quad \Omega \tag{10}$$

$$\text{suitable Dirichlet conditions in place of Equation (3) or (7) for both } \psi \text{ and } \omega \tag{11}$$

where $J \equiv 1$ if no co-ordinate transformation is involved. To resolve the further coupling from the boundary conditions, a simplified version of Equations (10)–(11) is introduced.

$$0 = \mathscr{L}\omega, \quad \mathscr{L}\psi = -\omega/J \quad \text{in } \Omega \tag{12}$$

$$\psi = 0, \quad \omega = \mathbf{w} \text{ on Dirichlet boundaries; plus periodic condition, if any} \tag{13}$$

The purpose of solving these Stokes-like problems with suitable Dirichlet data, **w**, will be clear as we proceed.

Let the indices, i and j, denote the generic collocation points on the boundaries where Dirichlet condition for ψ is specified, as shown in Equations (3) and (7). Denote by δ_{ij} the Kronecker function of these indices; that is $\delta_{ij}=0$ unless $i=j$, in which case $\delta_{ij}=1$. For each index i, we solve Equations (12)–(13) with Dirichlet data $\mathbf{w}=\delta_{ij}$. These solutions, $\{\omega_i,\psi_i\}$, are used to construct a matrix, $\mathscr{S}$, whose ith column records the pseudospectral approximation of the normal derivative of ψ_i on the Dirichlet boundaries. We shall call it a Stokes corrector, which is similar to the influence matrix employed in other numerical methods [10, 11]. We assume $\mathscr{S}$ is invertible here, but will give a correction in Section 4.

As the first application we employ the matrix, $\mathscr{S}$, to solve a particular case related to Equations (4)–(7). Namely, find ω^* and ψ^* such that

$$0=\mathscr{L}\omega^*,\quad \mathscr{L}\psi^*=-\omega^*/J\quad \text{in}\Omega \tag{14}$$

$$\psi^*(0,\eta)=\psi^*(2\pi,\eta)\quad\text{and}\quad \omega^*(0,\eta)=\omega^*(2\pi,\eta)\quad\text{on }\Gamma_3\cup\Gamma_4 \tag{15}$$

$$\psi^*=0\quad\text{on }\Gamma_1,\quad \psi^*=1\quad\text{on }\Gamma_2,\quad\text{and}\quad \partial\psi^*/\partial v=0\text{ on }\Gamma_1\cup\Gamma_2 \tag{16}$$

To this end, we first solve Equations (14)–(16) using the homogeneous Dirichlet condition on ω^* to replace the Neumann condition on ψ^*. Denote the solution by ω° and ψ°, and compute the vector of normal derivatives, $\mathbf{v}=\partial\psi^\circ/\partial v$, on $\Gamma_1\cup\Gamma_2$. Then solve Equations (12)–(13) with $\mathbf{w}=-\mathscr{S}^{-1}\mathbf{v}$. Adding the results to ω° and ψ° yields the wanted answer. This solution will yield two integral constants which are equal in theory, but can be slightly different in practice. So their sum is used:

$$\oint_{\Gamma_1}\partial\omega^*/\partial v+\oint_{\Gamma_2}\partial\omega^*/\partial v=p^*\neq 0 \tag{17}$$

Now we are ready to state the flow problem. Find Q such that $Q=F(Q)$, where $F(Q)$ is computed as follows.

Algorithm A

1. Given Q, solve Equations (10)–(11) with zero Dirichlet data. Denote the results by ω^0 and ψ^0, and compute the vector of normal derivatives, $\mathbf{v}=\partial\psi^0/\partial v$ on Dirichlet boundaries. Check it with the prescribed value, g, on Equations (3) or (7).
2. Solve Equations (12)–(13) with $\mathbf{w}=\mathscr{S}^{-1}(g-\mathbf{v})$. Denote the results by ω^1 and ψ^1.
3. Set $q=0$. If $\tilde{\Omega}$ is doubly connected, check the integrals in Equation (8) with $\omega=\omega^0+\omega^1$. Denote their sum by p, and, from Equations (14)–(17), set $q=-p/p^*$.
4. Let $\omega=\omega^0+\omega^1+q\omega^*$ and $\psi=\psi^0+\psi^1+q\psi^*$. Define $F(Q)=\psi_y\omega_x-\psi_x\omega_y$ or $\psi_\eta\omega_\xi-\psi_\xi\omega_\eta$, by pseudospectral collocation.

3. THE NUMERICAL METHOD

As discussed above, one key ingredient in Algorithm A is to solve single Poisson equation, like $\mathscr{L}\mathbf{x}=\mathbf{b}$, with entire Dirichlet or Dirichlet/periodic mixed boundary conditions. We solve this system iteratively by quasi-minimal residual method (QMR) [12]. Since the condition number of $\mathscr{L}$ increases rapidly with the number of collocation points, proper preconditioning

is needed. This is accomplished here by the finite-difference counterpart of $\mathscr{L}$, as described below.

Instead of using spectral polynomials, we approximate the first derivative in each spatial direction using the local, three-point Lagrange interpolations. These data are used to construct the local, three-point Hermite interpolations for obtaining the second derivatives. It leads to a five-point scheme in each spatial direction for approximating $\mathscr{L}$. This approach appears to be more effective as a preconditioner than that directly using five-point Lagrange interpolations, given the nonuniformity of the underlying grid.

Since our goal is to find the fixed point, $Q = F(Q)$, it is natural to employ the Picard iteration: $Q_{n+1} = F(Q_n)$ with some initial trial Q_0, and look forward to its convergence. This simple process, however, is fail-prone, given the complexity of the operator F as described by Algorithm A. We introduce below a workable modification.

Algorithm B

1. Let Q_n and Q_{n+1} be the two most recent iterants, whether $Q_{n+1} = F(Q_n)$ or not. Perform the following error minimization:

$$\min_{\mu \in [-\alpha, \alpha]} \mathscr{J}(\mu) \quad \text{where } \alpha = \mathcal{O}(1) \quad \text{and} \tag{18}$$

$$\mathscr{J}(\mu) = \|F(Q_n + \mu(Q_{n+1} - Q_n)) - (Q_n + \mu(Q_{n+1} - Q_n))\|^2 \tag{19}$$

   In Equation (19), $\|\cdot\|$ stands for the ℓ_2-norm over the collocation points. By going over the steps in Algorithm A, one can find that $\mathscr{J}(\mu)$ is a polynomial of degree four. Therefore the minimization can be done with ease.
2. Denote by μ_* the minimizer closest to 0, and let $Q_* = Q_n + \mu_*(Q_{n+1} - Q_n)$. Define $\rho_* = \|F(Q_*) - Q_*\| / \|F(Q_n) - Q_n\|$. If ρ_* is close to 1 (say, $\rho_* > 0.95$), a stagnant iteration is encountered; go to Step 3 for a cure. Otherwise make the updates: $n \leftarrow n+1$, $Q_n \leftarrow Q_*$, $Q_{n+1} \leftarrow F(Q_*)$, and go back to Step 1.
3. Pick at random a $\mu \in [-\alpha, \alpha]$, and set $Q_* = Q_n + \mu(Q_{n+1} - Q_n)$. Update Q_{n+1} only: $Q_{n+1} \leftarrow Q_n + (F(Q_*) - Q_*)$, and go back to Step 1.

In other words, those Q_n's according to Algorithm B form the modified Picard iterants. The error, $\|F(Q_n) - Q_n\|$, is non-increasing by design. Thanks to the random perturbation in Step 3 for sustaining the line search, a monotone decreasing is observed in numerical experiments. Note that we do not claim it is a global scheme; the alteration of search direction is mainly to get rid of saddle-like traps rather than well-like ones.

By experience from preliminary studies [13] and a previous work [7] based on finite-difference approach, Step 3 in Algorithm B is seldom invoked for flows with $Re < 100$. However, the hit rate of this step is about 30% for flow with $Re \sim 1000$. In either case the convergence can be greatly improved by casting Algorithm B into a multigrid fashion.

We adopt here the nonlinear full approximation scheme (FAS), as expounded by Brandt [14]. V-cycling and standard double coarsening on the collocation points are used. Only the prolongation, I_H^h, and restricition, I_h^H, need a further explanation. Let ϑ_H be any coarse grid function. The prolongation, $I_H^h \vartheta_H$, is directly derived from ϑ_H's pseudospectral interpolant. To be more shape-preserving, one can extend this interpolant's modal coefficients across the Nyquist bound by even and odd reflections for cos and sin modes, respectively. As a fact, this

information is ready in many Fourier transform packages. Then, a high-order low-pass filter is applied to these coefficients before turning them into nodal values. The family of filters with integer parameter $k \geqslant 4$:

$$\varphi_k(x) = 1 - \frac{1}{\sigma} \int_0^x \xi^k (1-\xi)^k \, \mathrm{d}\xi \quad \text{where } \sigma = \int_0^1 \xi^k (1-\xi)^k \, \mathrm{d}\xi \tag{20}$$

proposed by Vandeven [15] serves well for this purpose. On the other hand, the restriction, $I_h^H \vartheta_h$, of any fine grid function, ϑ_h, is obtained through least-squares principle. That is, $\|\vartheta_h - I_H^h(I_h^H \vartheta_h)\| = \text{minimum}$ in ℓ_2-norm over the fine-grid collocation points.

Note that we employ the same strategy to construct the multigrid version of the finite-difference preconditioned QMR iteration for the kernel Poisson solver in Algorithm A. Because of linearity FAS reduces to the usual correction scheme, and the intermediate relaxation in the fine-to-coarse branch of V-cycling can be saved. Namely, the cycling becomes sawtooth-like. Different choice of these spectral multigrid components can be found in the work by Zang *et al.* [16].

We conclude this section with a remark that applying a filtering to the estimations of Q and $F(Q)$ (i.e. Step 4 in Algorithm A) can accelerate the convergence of Algorithm B as well. See examples shown below.

4. WORKED EXAMPLES AND DISCUSSIONS

We shall first show the spectral accuracy of our scheme when it is applied to a class of flow problems where the analytic results are available to us. So, consider flow between two cylinders of which at least one has a constant rotation about its axis. The inner and outer cylinders have radii d_1 and d_2, respectively. Their centers are separated by a distance $0 \leqslant \lambda < d_2 - d_1$, and yield an eccentricity $\varepsilon = \lambda/(d_2 - d_1)$. The constant angular velocities are denoted by Θ_1 and Θ_2, respectively, and their signs indicate the senses of rotation (e.g. positive = clockwise). The Reynolds number Re is defined here as $Re = d_1^2|\bar{\Theta}|/\nu$, where $\nu =$ kinematic viscosity, and $\bar{\Theta} = \Theta_1$ unless $\Theta_1 = 0$, in which case $\bar{\Theta} = \Theta_2$. These flows are related to the lubrication studies of journal bearing.

Clearly, this is not a standard setting for applying pseudospectral methods. A co-ordinate transformation is made as follows. Let $z = x + iy$. The conformal mapping in terms of complex variable:

$$\zeta = \frac{z + c}{1 + cz} \quad \text{where } c = \frac{\beta}{1 + \sqrt{1 - \beta^2}} \quad \text{and} \quad \beta = \frac{2\lambda d_1}{d_2^2 - d_1^2 - \lambda^2} \tag{21}$$

transforms the cylinders into a concentric configuration in the ζ-plane. Let $\zeta = \exp(\tilde{\eta} - \mathrm{i}\tilde{\xi})$. The collocation points in the $\tilde{\xi}$ and $\tilde{\eta}$ directions are respectively determined by requiring them, after the inverse map $z = (\zeta - c)/(1 - c\zeta)$, uniformly located along the inner cylinder, and affinely similar to the Chebyshev abscissa along the radius spanning the widest gap between the cylinders. As shown in Figure 1, such a remeshing is used to alleviate the distortion on discretization brought about by eccentricity. Denote them by $\tilde{\xi} = \tilde{\xi}(\xi)$ and $\tilde{\eta} = \tilde{\eta}(\eta)$, we get Equations (4)–(8) in place.

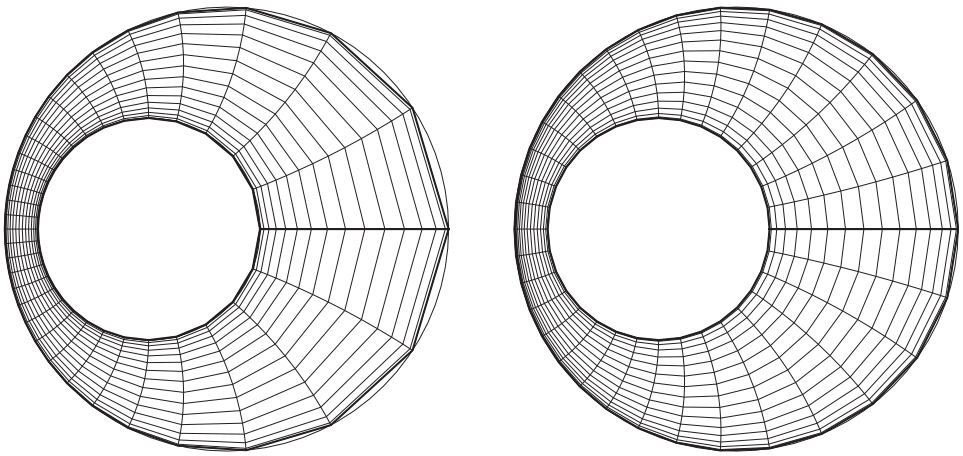

Figure 1. Layouts of the pseudospectral grid between two eccentric cylinders: (a) the usual one; and (b) that improved by remeshing. They have the same number of grid points, and are based on the conformal mapping mentioned in the text.

Table I. Configuration of eccentric rotating cylinders.

Case	d_1	d_2	λ	Θ_1	Θ_2
1	1	2	0.5	−1	0
2	1	2	0.5	0	−1
3	1	2	0.5	1	−0.5
4	1	2	0.7	−1	−0.5

The flow is examined under the settings summarized in Table I. We begin with computing the Stokes flow, i.e. $Re = 0$, for which the result can be compared with the analytic findings by Wannier [17] and Ballal and Rivlin [18]. To check the accuracy the numbers of the pseudospectral nodes in ξ and η directions are, respectively, equal to N and $N + 1$, where N ranges from 8 to 32. The base-10 logarithm of the maximum and root-mean-squares errors for the four cases listed in Table I are plotted against N in Figures 2(a–d) and 2(e–h), respectively. The spectral accuracy is demonstrated by the almost linear behaviour of these curves.

The central part of these computations lies in the Poisson solver, $\mathscr{L}\mathbf{x} = \mathbf{b}$. As discussed in Section 3, such a system is first preconditioned by a finite-difference approximation and then solved iteratively by QMR scheme in a multigrid fashion. Within each sawtooth-like cycle, the QMR scheme takes 3–4 iterations for each postsmoothing. We show its typical three-grid performance in Figure 3, by measuring the decay of $\log_{10}(\|\mathbf{b} - \mathscr{L}\mathbf{x}\|)$ against the cycling index. This is related to constructing the Stokes corrector matrix, $\mathscr{S}$, via Equations (12)–(13). The decays of ω- and ψ-residuals varying with the column indices of $\mathscr{S}$ are plotted together in Figures 3(a) and 3(b), respectively. Fast convergence is evident in view of their drops in each vertical direction.

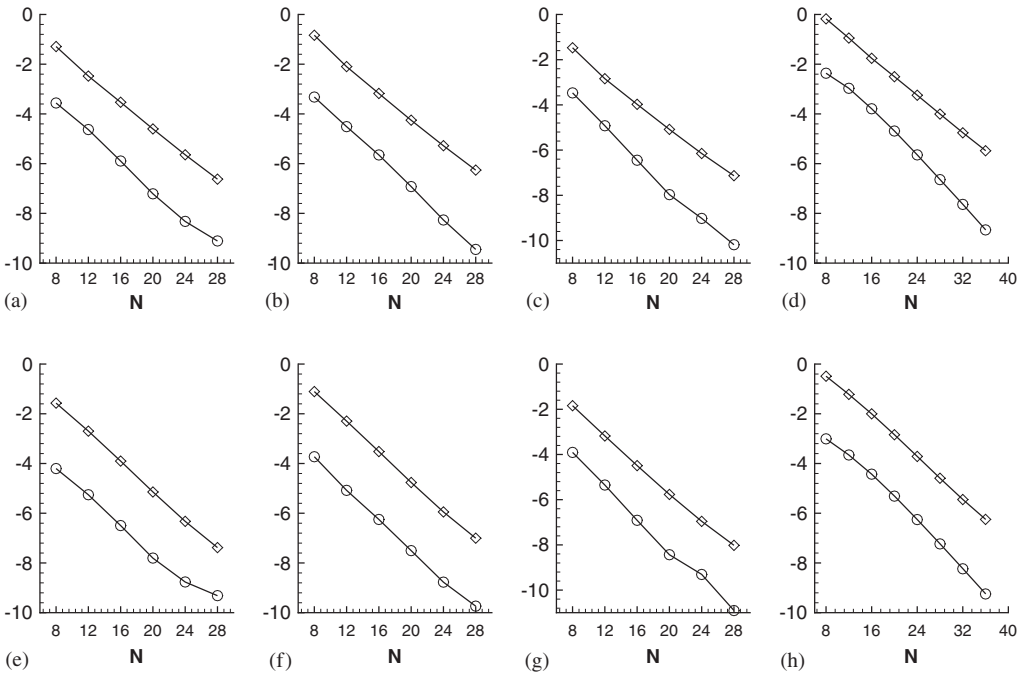

Figure 2. Base-10 logarithm of (a)–(d) maximum and (e)–(h) root-mean-squares errors against the number of pseudospectral nodes for flow cases list in Table I. –◇–, vorticity; –○–, streamfunction.

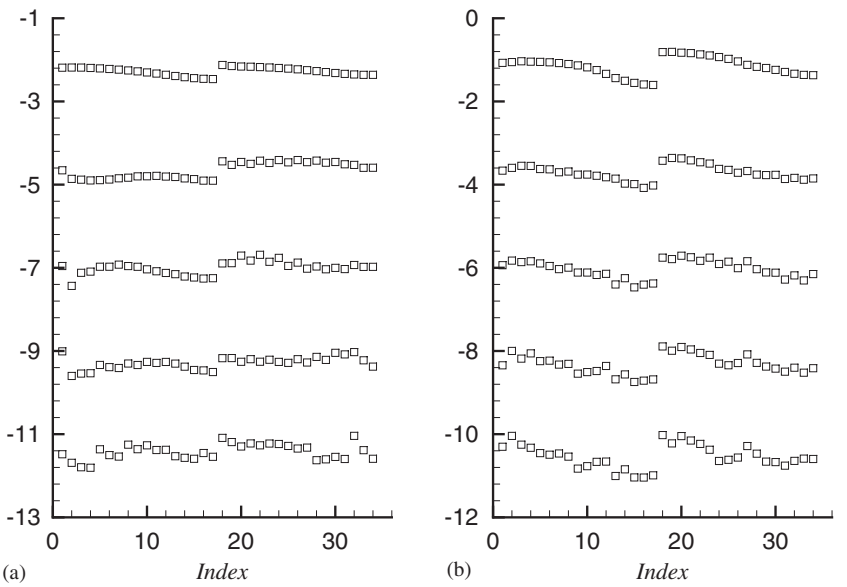

Figure 3. Three-grid Poisson solver with (a) ω- and (b) ψ-residuals of form $\log_{10}(\|\mathbf{b} - \mathscr{L}\mathbf{x}\|)$ dropping with the multigrid cycling index. They are related to constructing the matrix $\mathscr{S}$, and plotted together against column indices of $\mathscr{S}$.

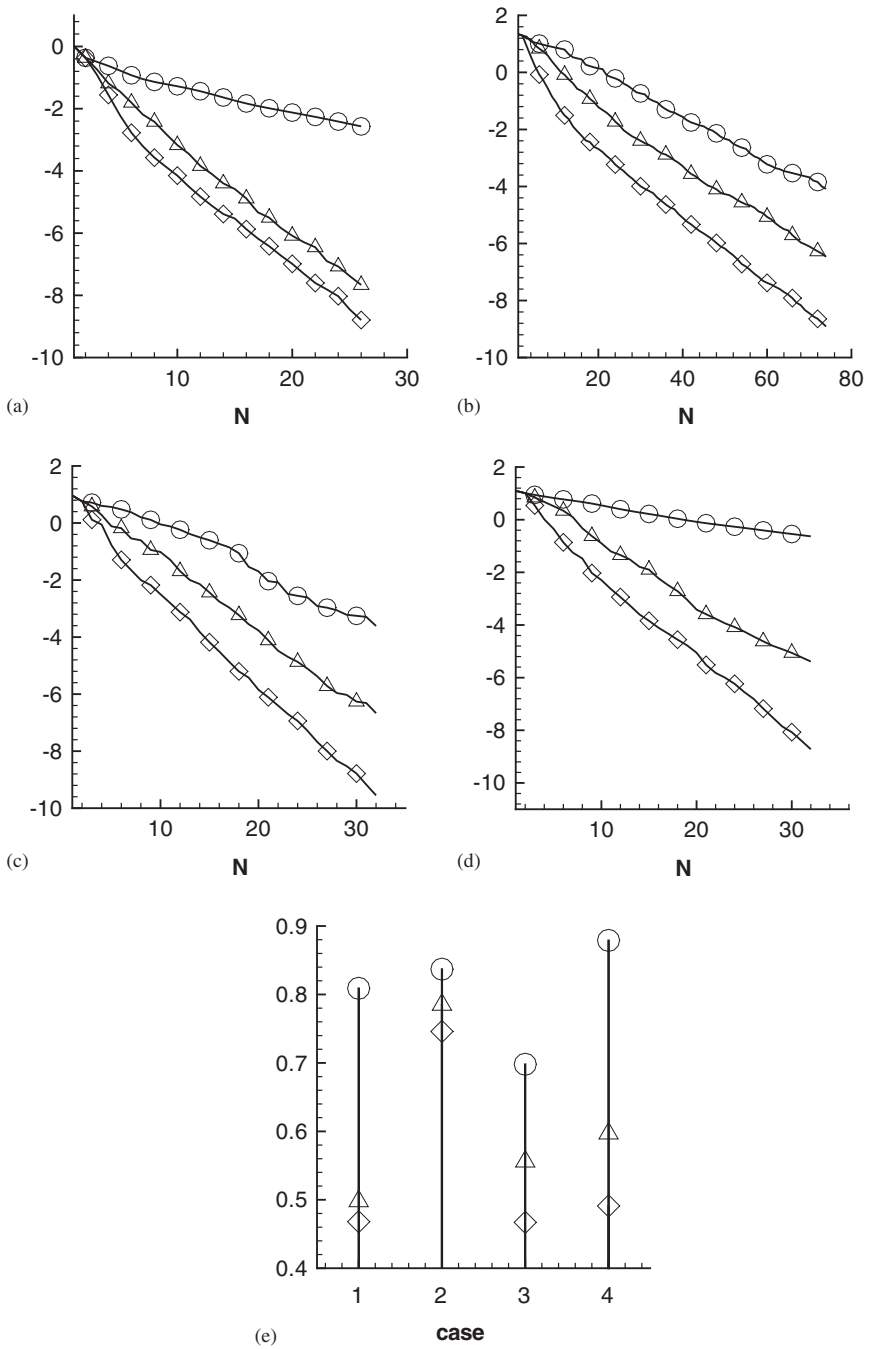

Figure 4. (a)–(d) Histories of $\log_{10}(\|F(Q_N) - Q_N\|)$ against multigrid cycling index N, in one (○)-, two (△)-, and three (◇)-grid iteration for flow cases listed in Table I; and (e) summary of the convergence rates.

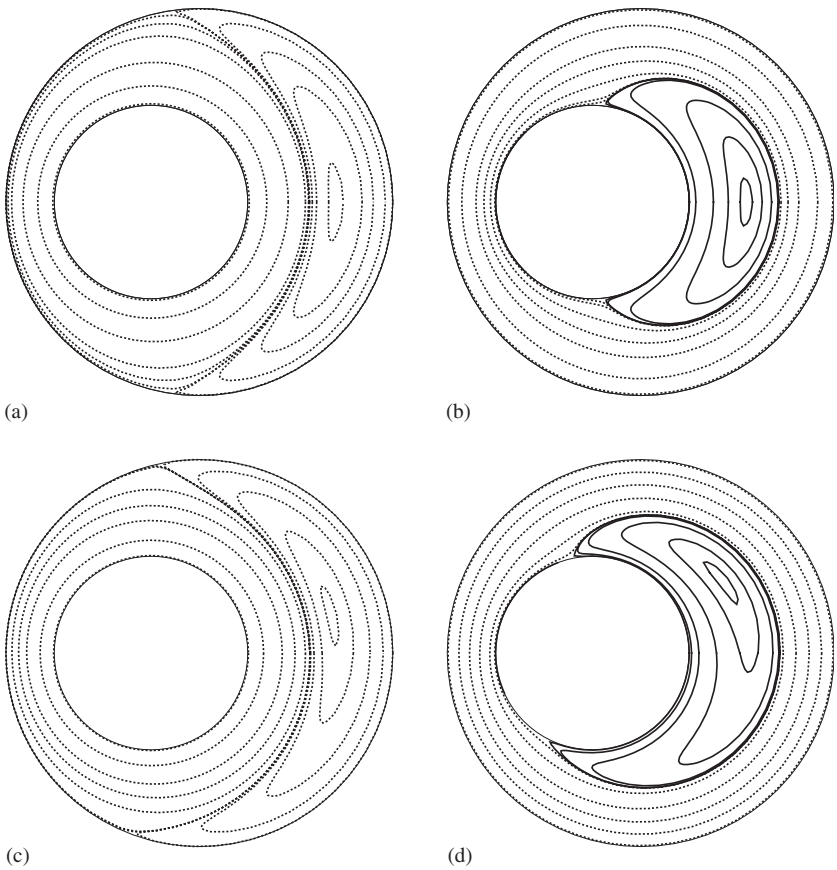

Figure 5. Streamlines (dashed on negative levels) for Cases 1 and 2 in Table I: (a)–(b) $Re = 0$; (c)–(d) $Re = 100$.

We then compute flows with $Re = 100$, using the corresponding Stokes flows as the initial guess. The numbers of the pseudospectral nodes in ξ and η directions are equal to 32 and 25, respectively. The convergence histories related to the one-, two-, and three-grid implementations of Algorithm B are shown in Figure 4(a–d) for the four cases listed in Table I, respectively. Within each V-cycle the line search or error minimization specified in Algorithm B is performed three times as the pre- and post-relaxation; the number of relaxations at coarser grid can be slightly increased. In each case the ℓ_2-norm, $\|F(Q_N) - Q_N\|$, decays exponentially with the multigrid cycling index, N, in proportion to σ^N for some constant, $0 < \sigma < 1$. We call this constant convergence rate, and the result is summarized in Figure 4(e).

The comparisons between the flows with $Re = 0$ and 100 are shown in Figures 5 and 6 for streamlines, and in Figures 7 and 8 for vorticity contours. Different types of recirculation region are formed, and closely related to the cylinders' rotation modes. Symmetry breaking is the apparent effect of convection on these regions. For each of them the locations such as the eddy center and the separation and reattachment points, however, do not always change in the direction parallel to the cylinder's rotation. They can depend on the Reynolds number. Such

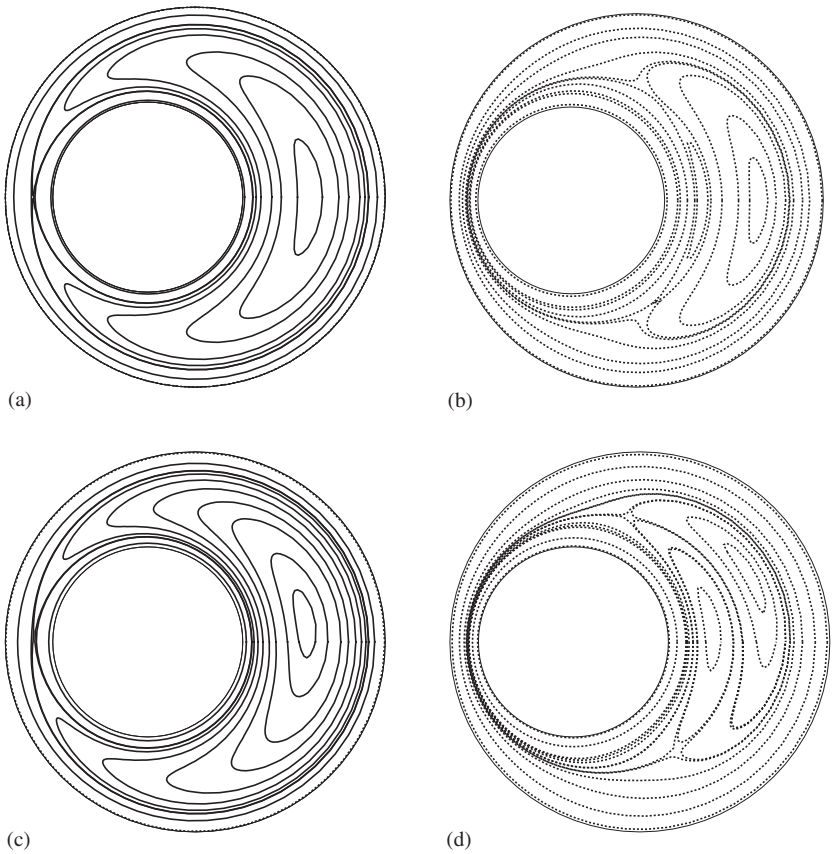

Figure 6. Streamlines for Cases 3 and 4 in Table I: (a)–(b) $Re = 0$; and (c)–(d) $Re = 100$.

a fact has been discussed, for example, by Ballal and Rivlin [18] and Chou [7], using a first-order perturbation or a finite-difference method. To provide a further evidence we compute the flows in Case 4 of Table I, for Reynolds number ranging from 0 to 100. The changes of the two eddies and their common closure points are shown in Figure 9. They also provide a quantitative improvement on our previous finite-difference work mentioned above.

Now, let us move on to the more standard setting: the lid-driven cavity flow. First and foremost, we encounter the singularity of the Stokes corrector matrix, $\mathscr{S}$, as constructed in Section 2. Numerically, the boundary conditions on the four corners are irrelevant to the flow calculation using a tensor-product-like, collocated discretization. So they are not involved in constructing $\mathscr{S}$. It is found that $\mathscr{S}$ still has a four-dimensional null space. If $\mathbf{w}$ in Equation (13) is chosen from this space, it gives a negligible solution to Equation (12). Such a fact, for example, has also been examined by Ehrenstein and Peyret [11]. Therefore the inverse, $\mathscr{S}^{-1}$, is interpreted here in terms of a variant of pseudoinverse mimicking the domain decomposition.

First we partition the boundary collocation points into two groups. Namely, the eight collocation points containing the four corners form one group, and the remaining points form the other. The restriction operators with respect to the former and latter groups are denoted

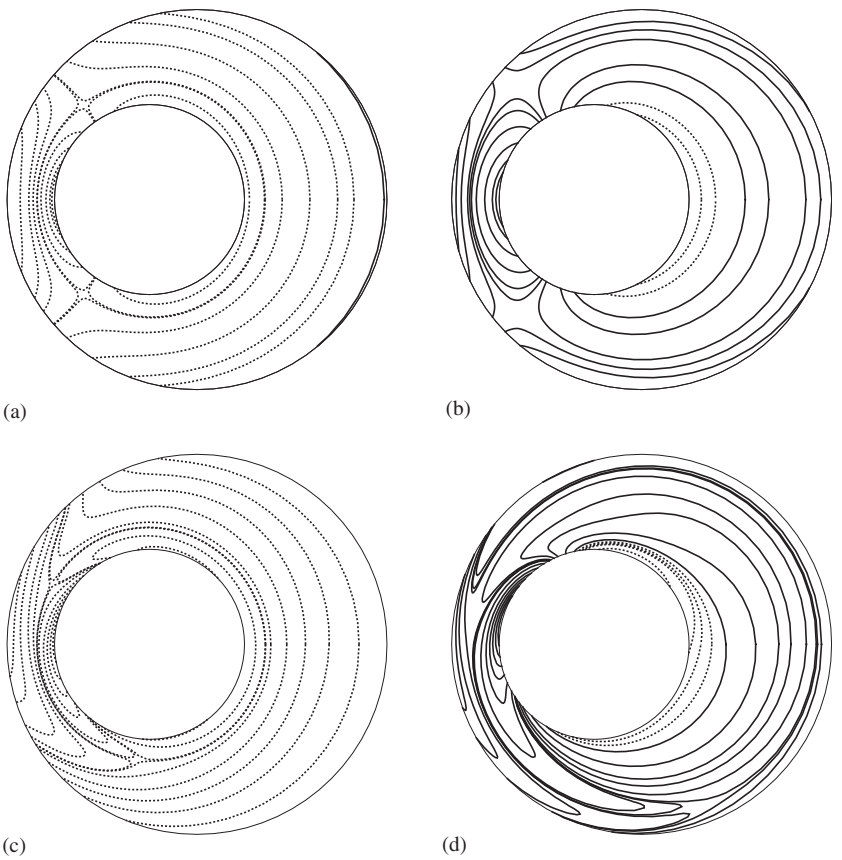

Figure 7. Vorticity contours (dashed on negative levels) corresponding to Figure 5.

by $\tilde{\mathscr{R}}$ and $\mathscr{R}$, respectively. Then the matrix, $\tilde{\mathscr{S}} = \mathscr{R}\mathscr{S}\mathscr{R}^{\top}$ where $\mathscr{R}^{\top}$ means the transpose of $\mathscr{R}$, is invertible. Denote the identity matrix by $\mathscr{I}$, and define

$$\mathscr{P} = \mathscr{R}^{\top}\tilde{\mathscr{S}}^{-1}\mathscr{R} \quad \text{and} \quad \mathscr{T} = \tilde{\mathscr{R}}\mathscr{S}(\mathscr{I} - \mathscr{P}\mathscr{S})\,\tilde{\mathscr{R}}^{\top} \tag{22}$$

where $\mathscr{T}$ is an 8×8 matrix, but of rank 4 only. The solution $\mathbf{w}$ to $\mathscr{S}\mathbf{w} = \mathbf{v}$ is obtained as $\mathbf{w} = \tilde{\mathscr{R}}^{\top}\mathbf{w}_1 + \mathscr{R}^{\top}\mathbf{w}_2$ where

$$\mathscr{T}\mathbf{w}_1 = \tilde{\mathscr{R}}(\mathscr{I} - \mathscr{S}\mathscr{P})\mathbf{v} \quad \text{by means of pseudoinverse} \tag{23}$$

$$\mathbf{w}_2 = \tilde{\mathscr{S}}^{-1}\mathscr{R}\,(\mathbf{v} - \mathscr{S}\tilde{\mathscr{R}}^{\top}\mathbf{w}_1) \tag{24}$$

As obtained by Equations (22)–(24) the Dirichlet boundary data, $\mathbf{w}$, for the vorticity Poisson equation presents irregularity around the corners of the cavity, if a constant speed is specified on the driven lid. To be amenable to the pseudospectral approximation, a regularized version is used. Namely, the constant function $v \equiv 1$ is replaced by $v = (1 - x^2)^2$, for $-1 \leqslant x \leqslant 1$. It has been shown by Shen [19] that this model has qualitative features similar to the original one.

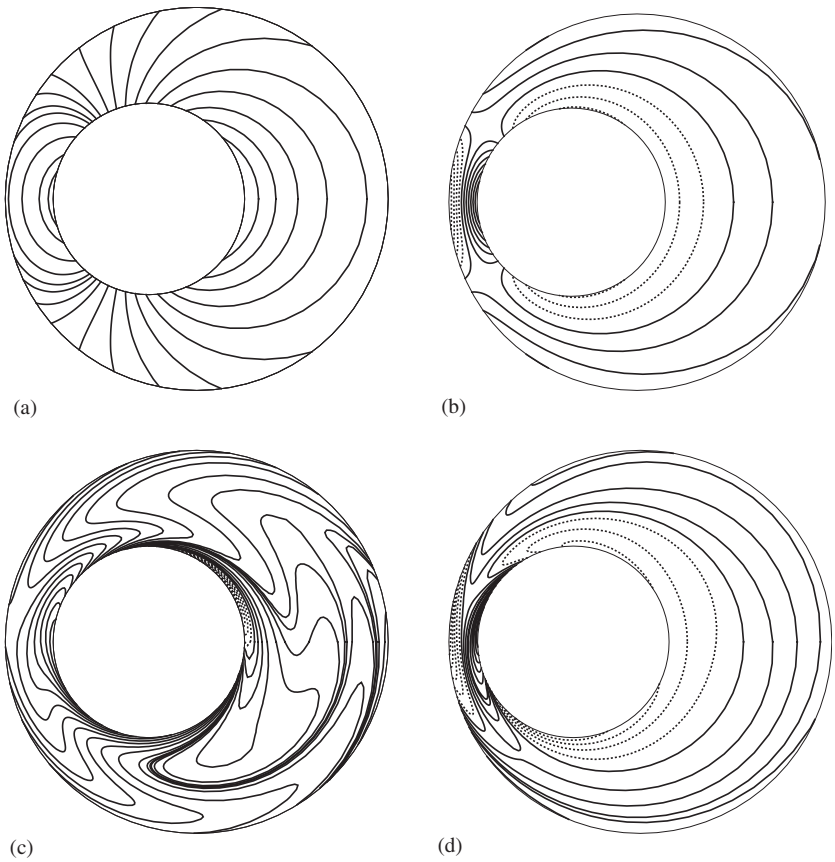

Figure 8. Vorticity contours corresponding to Figure 6.

In the following we want to demonstrate the computations of flows with a Reynolds number like $Re = 0, 100$, and iteratively doubled till $Re = 1000$. Each latter case use the previous one as the initial guess. The numbers of the pseudospectral nodes in ξ and η directions are both equal to 37. Figure 10(a–e) present the convergence histories related to the one-, two-, and three-grid implementations of Algorithm B against the multigrid cycling index; their convergence rates are summarized in Figure 10(f). Note that these rates are not sensitive to initial guesses, which mainly influence the initial residuals.

In view of Figure 10, a monotone convergence also holds in these computations where the random perturbation introduced in Step 3 of Algorithm B plays an important role. Without it the algorithm gets stuck within few iterations, especially when Re is large. To demonstrate this, let each call to Algorithm B correspond to an entry of a matrix. This entry will be marked with an asterisk($*$) if Step 3 of Algorithm B is not invoked; otherwise it is left blank. Figure 11 shows for $Re = 1000$ the appearances of these matrices for each of the one-, two- and three-grid implementations. The percentage of blanks in each matrix is called the hit rate of random perturbation. In view of Figure 11(c) this rate will increase if the flow is poorly represented on the coarsest grid.

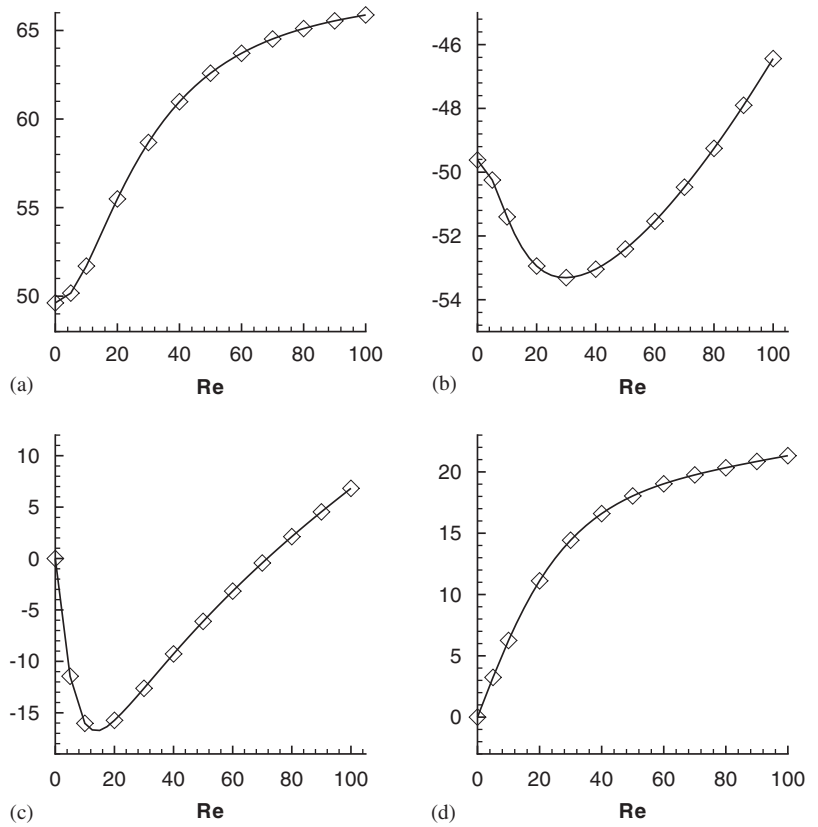

Figure 9. Polar angles (in degree) of stagnation points varying with *Re* in Case 4 of Table I: (a) upper and (b) lower closure points; (c) inner and (d) outer eddy centers.

In addition to the development along the sides of the cavity, the vorticity field around the cavity center also tends to develop richer structure for flow with higher Reynolds number. This happening does not well match the distribution of Chebyshev collocation points. Therefore we see the slowdown of the convergence rate in Figure 10(f). Nevertheless, we get the solution with ℓ_2-norm error less than 10^{-10} in a few tens of iterations. The same accuracy would be achieved by other methods [19, 20] in a few hundreds or even a few thousands of time steps, where cheaper operations are possible in each step.

The computed flow patterns are shown in Figure 12(a–c) for streamlines, and in Figure 12(d–f) for vorticity contours. The centers of the primary and secondary vortices appearing in Figure 12(a–c) are located and plotted in Figure 13, together with the measurements by some other researchers employing a spectral or pseudospectral approach [19–21]. Good agreement is found in the trend of these locations against the Reynolds number.

Finally, we discuss a filtering effect on the estimation of the convection term, $\psi_y\omega_x - \psi_x\omega_y$ or $\psi_\eta\omega_\xi - \psi_\xi\omega_\eta$. Such a filtering is intended to be used in Algorithm B in conjunction with the finest grid only. Parallel to the direction of differentiation a high-order low-pass filter is

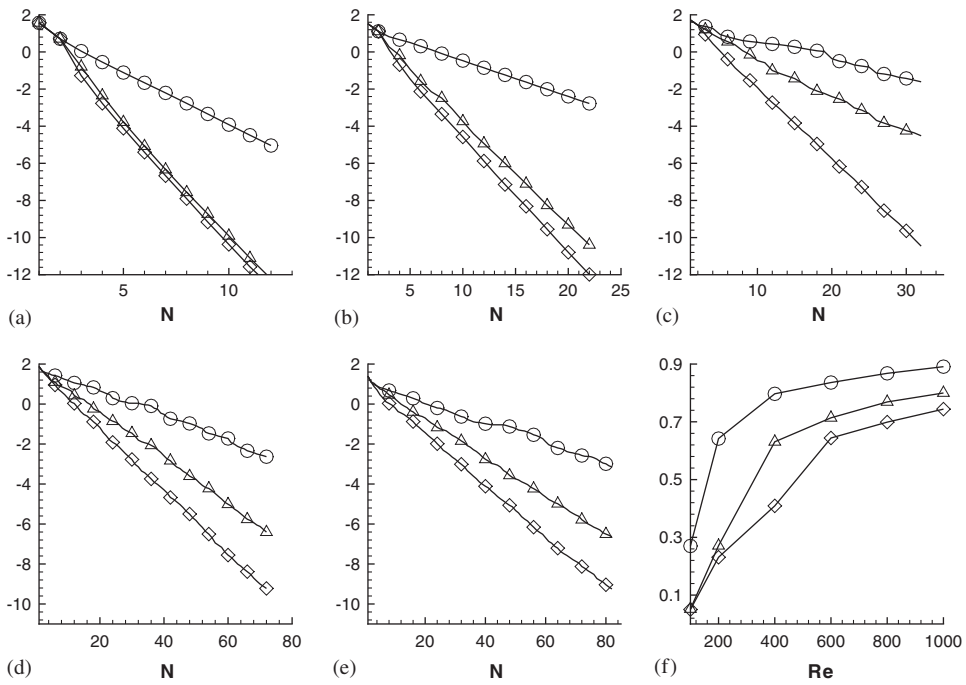

Figure 10. Histories of $\log_{10}(\|F(Q_N) - Q_N\|)$ against multigrid cycling index N, in one ($\circ$)-, two ($\triangle$)-, and three ($\diamond$)-grid iteration for regularized lid-driven cavity flows. (a)–(e) $Re = 100, 200, 400, 800$ and 1000, respectively; and (f) summary of the convergence rates.

applied to the modal coefficients of each individual pseudospectral interpolant, before turning these coefficients into nodal values. As shown in Equation (20), the filter family proposed by Vandeven [15] is employed here.

The phenomena of monotone convergence hold whether or not this filtering is activated. However, the filtered version can converge at a speed 2.5 to 4 times faster than the unfiltered one, as shown in Figure 14(a–c) for $Re = 200$, 400, and 1000, respectively. For each of these Reynolds numbers the two versions of solutions have a relative difference, in ℓ_2-norm, less than 0.6, 1.1 and 3%, respectively. It leads to the conclusion that suitable filtering is favourable in conjunction with collocation approach, when the original pseudospectral resolution is finite but reasonably good.

5. CONCLUSION

We have proposed a multigrid pseudospectral method to simulate steady flows. These flow problems are cast into a fixed-point formulation, and solved by a Picard-like iteration. The success of this scheme lies in three crucial factors. Namely, one-dimensional error minimization, random perturbation for sustaining the line search, and multigrid implementation. Worked examples fall into two categories. That is flow between two eccentric rotating cylinders, which

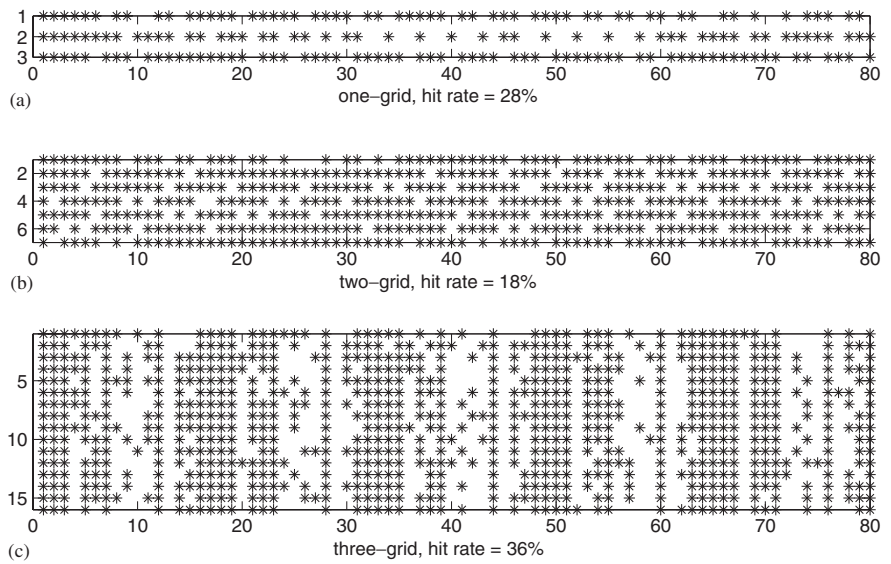

Figure 11. The occurence of random perturbations represented by blank spots in matrices recording all calls to Algorithm B. (a)–(c): one-, two- and three-grid implementation, respectively.

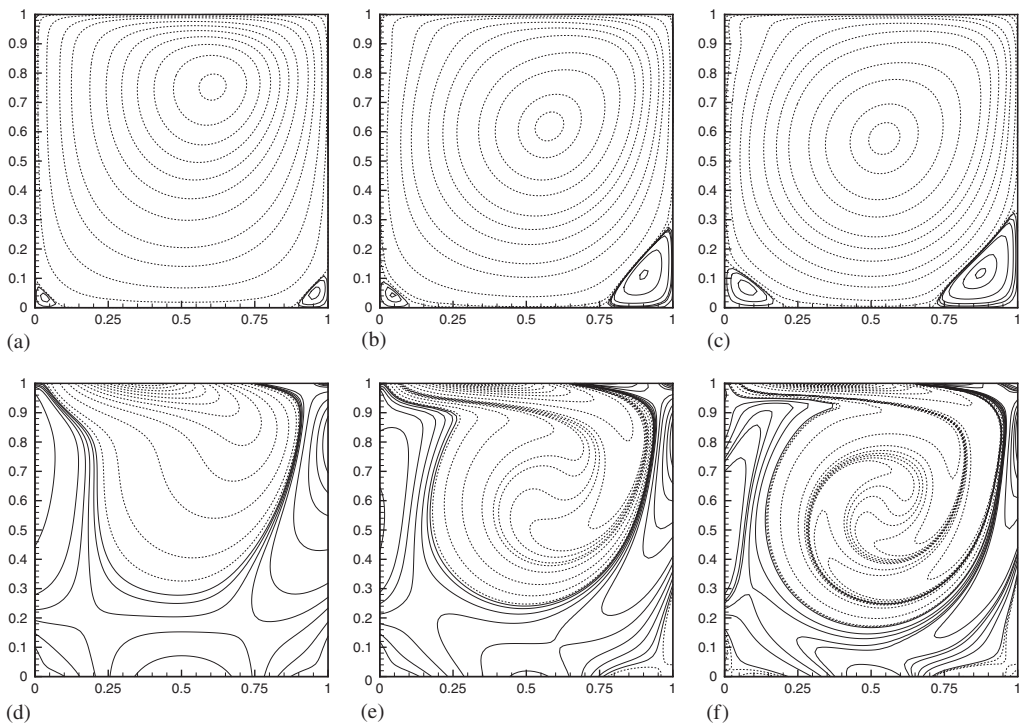

Figure 12. (a)–(c) streamlines and (d)–(f) vorticity contours (dashed on negative levels) for cavity flows with $Re = 100,\ 400$ and 1000, respectively.

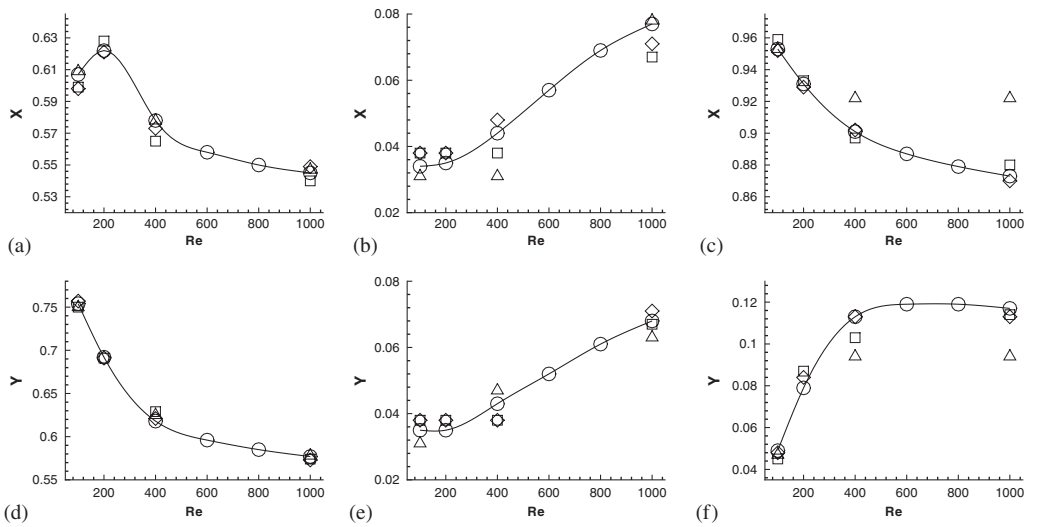

Figure 13. *Re*-dependence of (a)–(c) x- and (d)–(f) y-co-ordinates of the primary, left secondary, and right secondary vortex centers of cavity flows. Symbols (△, □, ◇) correspond to References [19–21].

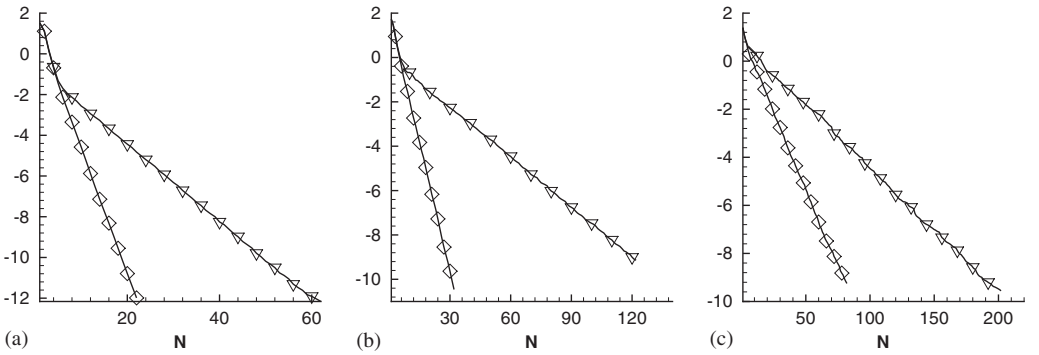

Figure 14. Comparisons of convergence between estimating Q with (◇) and without (▽) filtering for cavity flows; (a)–(c) $Re = 200,\ 400$ and 1000, respectively.

demonstrates the scheme's efficacy in a setting not standard to pseudospectral methods; and flow in a regularized lid-driven cavity, which demonstrates the scheme's efficacy in dealing with strong convection.

ACKNOWLEDGEMENTS

This research work was supported in part by the National Science Council under the grant NSC90-2115-M-001-011.

REFERENCES

1. Chorin AJ. A numerical method for solving incompressibe viscous flow problems. *Journal of Computational Physics* 1967; **2**:12–26.
2. Peyret R, Taylor TD. *Computational Methods for Fluid Flow*. Springer: New York, 1983.
3. Gresho PM, Sani RL. *Incompressible Flow and the Finite Element Method*. John Wiley & Sons: New York, 1998.
4. Ferziger JH, Perić M. *Computational Methods for Fluid Dynamics*. Springer: Berlin, 1999.
5. Canuto C, Hussaini MY, Quarteroni A, Zang TA. *Spectral Methods in Fluid Dynamics*. Springer: New York, 1988.
6. Peyret R. *Spectral Methods for Incompressible Viscous Flow*. Springer: New York, 2002.
7. Chou MH. A multigrid finite difference approach to steady flow between eccentric rotating cylinders. *International Journal for Numerical Methods in Fluids* 2000; **34**:479–494.
8. Gottlieb D, Orszag SA. *Numerical Analysis of Spectral Methods*. SIAM: Philadelphia, 1977.
9. Fornberg B. *A Practical Guide to Pseudospectral Methods*. Cambridge University Press: Cambridge, 1998.
10. Kleiser L, Schumann U. Treatment of incompressibility and boundary conditions in 3-D numerical spectral simulations of plane channel flows. In *Proceedings of the 3rd GAMM Conference on Numerical Methods in Fluid Mechanics*, Hirschel EH (ed.). Vieweg: Braunschweig, 1980; 165–173.
11. Ehrenstein U, Peyret R. A Chebyshev collocation method for the Navier–Stokes equations with applications to double-diffusive convection. *International Journal for Numerical Methods in Fluids* 1989; **9**:427–452.
12. Freund RW, Nachtigal NM. QMR: A quasi-minimal residual method for non-Hermitian linear systems. *Numerische Mathematik* 1991; **60**:315–339.
13. Chou MH. On flow simulation and multigrid acceleration. *NCTS Workshop on Multiscale Analysis and Computation* 2002 (June); National Center for Theoretical Sciences, Taiwan.
14. Brandt A. Guide to multigrid development. In *Multigrid Methods*, *Lecture Notes in Mathematics*, vol. 960, Hackbush W, Trottenberg U (eds). Springer: Berlin, 1982; 220–312.
15. Vandeven H. Family of spectral filters for discontinuous problems. *Journal of Scientific Computing* 1991; **6**(2):159–192.
16. Zang TA, Wong YS, Hussaini MY. Spectral multigrid methods for elliptic equations II. *Journal of Computational Physics* 1984; **54**:489–507.
17. Wannier GH. A contribution to the hydrodynamics of lubrication. *Quarterly of Applied Mathematics* 1950; **8**(1):1–32.
18. Ballal BY, Rivlin RS. Flow of Newtonian fluid between eccentric rotating cylinders: inertial effects. *Archive for Rational Mechanics and Analysis* 1976; **62**:237–294.
19. Shen J. Hopf bifurcation of the unsteady regularized driven cavity flow. *Journal of Computational Physics* 1991; **95**:228–245.
20. Phillips TN, Roberts GW. The treatment of spurious pressure modes in spectral incompressible flow calculations. *Journal of Computational Physics* 1993; **105**:150–164.
21. Pinelli A, Vacca A. Chebyshev collocation method and multidomain decomposition for the incompressible Navier–Stokes equations. *International Journal for Numerical Methods in Fluids* 1994; **18**:781–799.

